

Cite this: *J. Mater. Chem. A*, 2021, 9, 5780

Stabilization of ultra-small gold nanoparticles in a photochromic organic cage: modulating photocatalytic CO₂ reduction by tuning light irradiation†

Ashish Singh,  ‡ Parul Verma,  ‡ Debabrata Samanta,  Anupam Dey, Jyotirmoy Dey and Tapas Kumar Maji  *

Synthesis and stabilization of ultra-small metal nanoparticles (MNPs) composed of a few atoms are of paramount importance in modulating their material properties based on quantum confinement effects. The highly reactive surface of small MNPs tends to aggregate, resulting in bigger particles and subsequent deterioration of the catalytic activity. In this work, we exploited a dithienylethene (DTE) based photochromic organic cage (TAE-DTE) for the *in situ* stabilization of ultra-small Au NPs (Au@TAE-DTE) (<2 nm) through a unique “reverse double-solvent approach (RDSA)”. The Au@TAE-DTE showed similar photochromic properties to the TAE-DTE and shuttled between two metastable photoisomers, Au@TAE-DTE-O and Au@TAE-DTE-C, based on DTE ring opening and closing upon treating with visible and UV-light, respectively. The Au@TAE-DTE hybrid showed visible light ($\lambda = 400\text{--}750$ nm) driven catalytic activity for photochemical CO₂ reduction to CO. Importantly, irradiating with light of the full range ($\lambda = 250\text{--}750$ nm) allowed for co-existence of both photoisomers which thereby showed wide spectrum absorption as compared to individual photoisomers, consequently displaying substantially enhanced performance for the photocatalytic CO₂ reduction. Further, the real-time progress of the CO₂ reduction reaction and corresponding reaction intermediates was detected by an *in situ* DRIFT experiment.

Received 16th December 2020
Accepted 24th January 2021

DOI: 10.1039/d0ta12195a

rsc.li/materials-a

Introduction

The synthesis and stabilization of ultrasmall metal nanoparticles (MNPs) or nanoclusters (MNCs) have gained considerable attention in recent years owing to their wide range of applications in the field of catalysis, photophysics, chemical biology and therapeutics.^{1–3} The performances of MNPs are mainly size dependent due to the “quantum size effect”^{3–8} and small MNPs (<2 nm) are considered to be in the boiling state because of their high surface free energy and therefore show enhanced catalytic activity as compared to the large MNPs (>2 nm).^{4,8} In contrast, small MNPs tend to aggregate and consequently hinder the catalytic activity as well as stability in prolonged reactions. In general, porous materials having functionalized pore surfaces such as metal/covalent organic frameworks (MOFs/COFs), silica-based materials and various capping agents are being employed for the growth and

stabilization of MNPs.^{5,9–13} However, the large pore sizes of MOFs/COFs are often associated with the drawbacks of irregular distribution, leaching, and regrowth of MNPs eventually leading to suppressed performance of MNPs.¹⁴ Thus, stabilization of ultrasmall MNPs (<2 nm) is a challenging task which impedes their application in the domain of catalysis.

Recently, discrete organic cages (OC) bearing guest accessible cavities have emerged as promising candidates for stabilization of ultrasmall sized MNPs.^{15–19} Xu and co-workers demonstrated an excellent method called the “reverse double-solvent approach (RDSA)” for *in situ* stabilization of ultra-fine Pd NPs in organic cages and the resulting hybrid showed high dispersibility and ability to catalyze organic reactions efficiently.¹⁷ Similarly, we envisioned that the stabilization of ultrafine gold NPs in an organic cage¹⁵ using the RDSA could be a novel pathway to develop visible-light-driven photocatalysts for the CO₂ reduction reaction.¹⁶

It is noteworthy that photochemical CO₂ reduction to solar fuels with high selectivity and efficiency has been an intense research topic in recent times as it does not only address global warming but also provides a long-term solution for the shortage of energy and carbon resources.^{20–24} However, this is a complex process where multiple electron and proton transfers are involved and therefore poses significant challenges to the

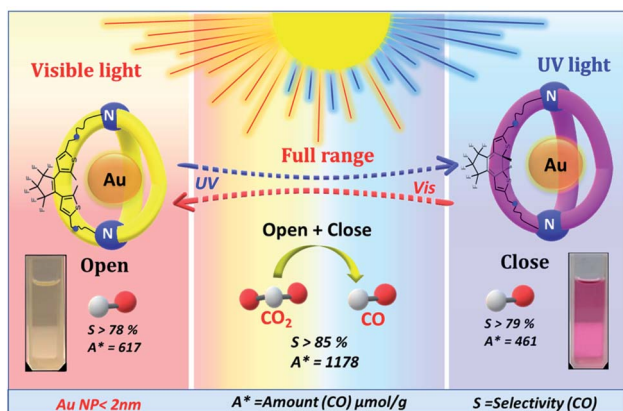
Molecular Material Laboratory, Chemistry and Physics of Material Unit, School of Advanced Materials (SAMat), Jawaharlal Nehru Centre for Advanced Scientific Research, Jakkur, Bangalore-560064, India. E-mail: tmaji@jncasr.ac.in; Web: <http://www.jncasr.ac.in/tmaji>

† Electronic supplementary information (ESI) available. See DOI: 10.1039/d0ta12195a

‡ These authors contributed equally.

researcher towards developing materials for photocatalytic CO₂ reduction with high efficiency and selectivity.^{25–28} To this end, discrete organic cages that can absorb visible light, exhibiting high dispersibility, could be an elegant design to display impressive photocatalytic activity towards CO₂ reduction.^{29,30} In this context, photochromic organic cages (POCs) could be an ideal system for realizing photocatalytic properties as they exhibit a broad absorption from UV to the visible region as a result of photo-responsive isomerization.^{29,31–37} Thus, photocatalytic activities of such photochromic cages can be influenced by modulating the irradiation light.³⁸ Further, owing to small cavity sizes, suitably functionalized POCs can act as a template for stabilization of ultra-small metal nanoparticles (NP@POCs) (example; Ag, Au and Cu) using the RDS approach.⁵ These NP@POC hybrids will not only provide catalytic sites but also enhance the light-absorbing properties owing to their localized surface plasmon band in the visible region, thereby enhancing the photocatalytic activity.¹⁷ Importantly, the photocatalytic activity of organic cages towards CO₂ reduction is under-explored and needs to be developed rationally.³⁹

In this work, we have exploited a dithienylethene (DTE) based photochromic organic cage²⁷ (Scheme 1, Fig. 1a), namely TAE-DTE, for the *in situ* stabilization of ultra-small Au nanoparticles (<2 nm) through a reverse double-solvent approach (RDSA).^{17,40,41} Interestingly, the size of Au NPs in the TAE-DTE cage was found to be approximately 1.3 nm which was significantly smaller than that in an earlier report.²⁹ The gold nanocomposite (Au@TAE-DTE) showed photochromism similar to the bare cage and displayed distinguished UV-Vis absorption spectra for their metastable photo-isomers. Next, the photo-isomer, Au@TAE-DTE-O (DTE open form), showed appreciable visible-light-driven photocatalytic activity for CO₂ reduction to CO (rate = 56 μmol g⁻¹ h⁻¹, selectivity >78%). More importantly, co-existence of both photoisomers, Au@TAE-DTE-O and Au@TAE-DTE-C (DTE closed form), in full-range light (250–750 nm) displayed wide absorbance and therefore activity and selectivity towards photocatalytic CO₂ reduction was increased significantly (rate = 105 μmol g⁻¹ h⁻¹, selectivity >85%). The



Scheme 1 Schematic representation of a photochromic organic cage and stabilization of ultra-small gold nanoparticles toward visible light driven photocatalytic CO₂ reduction with the hybrid cage material.

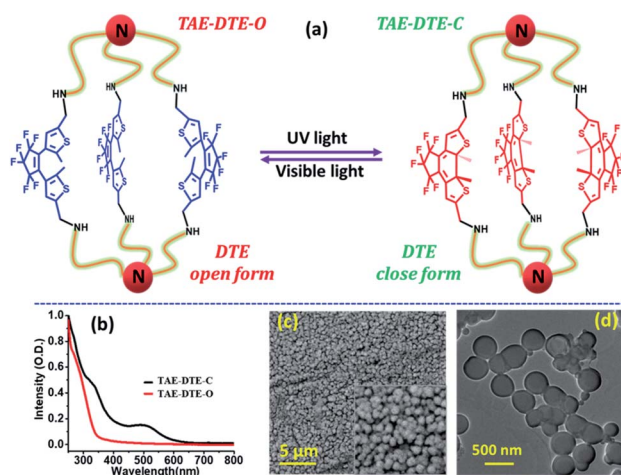


Fig. 1 (a) Photo-isomers (TAE-DTE-O and TAE-DTE-C) of the photochromic organic cage. (b) UV-Vis spectra in acetonitrile (10⁻⁵ M). (c) FESEM and (d) TEM image for TAE-DTE-O.

real-time progress of the CO₂ reduction reaction has been tracked by *in situ* Diffuse Reflectance Infrared Fourier Transform (DRIFT) spectroscopic study.

Results and discussion

Synthesis and characterization of the photochromic organic cage (TAE-DTE) was reported recently,²⁹ and we have followed a similar procedure with slight modification (see the ESI, Scheme S1 & S2†). In brief, the TAE-DTE cage was synthesized *via* Schiff base condensation between 4,4'-(perfluorocyclopent-1-ene-1,2-diyl)bis(5-methylthiophene-2-carbaldehyde) (DTE-dialdehyde) and 2,2',2''-triaminotriethylamine (TAE) followed by reductive amination using concentrated aqueous NaBH₄ (see the ESI† for details). The POC was characterized using various spectroscopic techniques, and the characterization data were found to be in good agreement with the literature report (see the ESI, Fig. S1–S4†).²⁹ The TAE-DTE-O formed an ultra-fine stable dispersion in common organic solvents (chloroform, methanol and ethyl acetate) as confirmed by the Tyndall effect (Fig. S5†). Notably, this dispersion cannot be distinguished by the naked eye and looks similar to the solution state (Fig. S5†). However, a poor dispersion was observed in water due to the presence of hydrophobic perfluoro substitutions on the exterior surface.⁴² Field Emission Scanning Electron Microscopy (FE-SEM) studies of the TAE-DTE-O showed the nano spherical morphology (100–150 nm) which was further supported by Transmission Electron Microscopy (TEM) analysis (Fig. 1c and d). PXRD measurements showed a broad peak at $2\theta = 18.5^\circ$ (4.79 Å), suggesting the absence of long-range ordering in the TAE-DTE-O cage (Fig. S6†).

The yellow coloured TAE-DTE-O changed to pink coloured photoisomers (TAE-DTE-C) upon UV irradiation for 10 seconds due to DTE ring-closing and the opposite was achieved upon visible light irradiation for 25 seconds as a result of DTE ring opening (Fig. 1a). UV-Vis spectra for both the photoisomers (10⁻⁵ M) were recorded in acetonitrile and found to be similar

to the literature report.²⁹ TAE-DTE-O showed broad absorbance in the UV-region (250–330 nm), whereas TAE-DTE-C showed additional absorption in the visible region (450–580 nm) with an absorption maximum at 520 nm (Fig. 1b). The optical HOMO–LUMO band gap was calculated from the Tauc plot derived from the absorption spectra and found to be 3.15 eV for TAE-DTE-O and 2.25 eV for TAE-DTE-C (Fig. S7†). Next, the quantum efficiency for the conversion of TAE-DTE-O to TAE-DTE-C and *vice versa* upon UV and visible light irradiation was calculated to be 62% and 53%, respectively (see the ESI, Fig. S8–S9†). The maximum conversion of TAE-DTE-O to TAE-DTE-C in the photo-stationary state (PSS) was observed to be 77.4%. The PXRD pattern and FE-SEM and TEM images of TAE-DTE-C were found to be similar to those of the TAE-DTE-O (Fig. S6 & S10†). Further, an optimized structure was computed for both TAE-DTE-O and TAE-DTE-C (Fig. S11 & S12†). The time-dependent density functional theoretical (TD-DFT) computation, at the D3-B3LYP/6-31G(d) level, suggested that the TAE-DTE-O was found to be stabilized by 54 kcal mol⁻¹ as compared to the TAE-DTE-C. The HOMO–LUMO band gap for the TAE-DTE-O was calculated to be 3.66 eV which was reduced significantly to 2.72 eV for the TAE-DTE-C (Fig. S13†). The UV-Vis transition in TAE-DTE-O ($I_{\max} = 290$ nm) appeared due to $\pi \rightarrow \pi^*$ electronic transition from the HOMO–1 to the LUMO+2 (296 nm, $f = 1.07$) (Fig. S11†). In addition to this type of transition, TAE-DTE-C also exhibited a low-energetic $\pi \rightarrow \pi^*$ transition at 537 nm from the HOMO to the LUMO with relatively lower intensity ($f = 0.24$) (Fig. S12†).

Next, we attempted *in situ* growth and stabilization of ultra-small gold nanoparticles (Au NPs) (<2 nm) in the TAE-DTE-O

cage using the RDSA, aiming to exploring the photocatalytic activity of the hybrid material towards CO₂ reduction (Fig. 2a).⁴³ In the RDSA, TAE-DTE-O (55 mg) possessing hydrophobic cavities was dispersed in water (10 ml), and the metal precursor (AuCl₃·6H₂O) (15 mg) was dissolved in a hydrophobic solvent (CH₂Cl₂) (15 μ l) and added to the TAE-DTE-O dispersion. The reaction mixture was stirred for 3 h. The metal precursor reached inside the POC through hydrophobic–hydrophobic interactions between the metal solution and POC cavity. Finally, the reaction mixture was treated with highly concentrated aqueous NaBH₄ (30 mg in 100 μ l) and further stirred for 3 h. This resulted in the reduction of metal ions (Au³⁺) to ultra-fine Au nanoparticles. Interestingly, the Au@TAE-DTE-O hybrid also formed a stable and fine dispersion similar to the POC as confirmed through the Tyndall effect (Fig. 2b and S14†). The PXRD pattern of Au@TAE-DTE-O showed a distinguishable peak at 38.9°, which confirmed the presence of gold NPs in the cubic phase (Fig. S15†).⁴⁴ The FT-IR spectrum of Au@TAE-DTE-O was observed to be similar to that of the TAE-DTE-O cage, suggesting non-covalent stabilization of Au NPs in the POC (Fig. S16†). The loading amount of Au in the Au@TAE-DTE-O hybrid was determined by inductively coupled plasma-atomic emission spectroscopy (ICP-AES) and found to be 2.2 wt%. The high-resolution TEM (HR-TEM) image indicated the uniform distribution of ultrasizes of Au NPs (<2 nm) on spheres (Fig. 2d and e). Notably, lattice fringes of 0.213 nm were observed in HRTEM images, indicating the orientation of cubic Au NPs in the (111) plane (Fig. 2e).⁴⁴ The high-angle annular dark-field scanning transmission electron microscopy (HAADF-STEM) image of Au@TAE-DTE-O hybrid also showed spherical

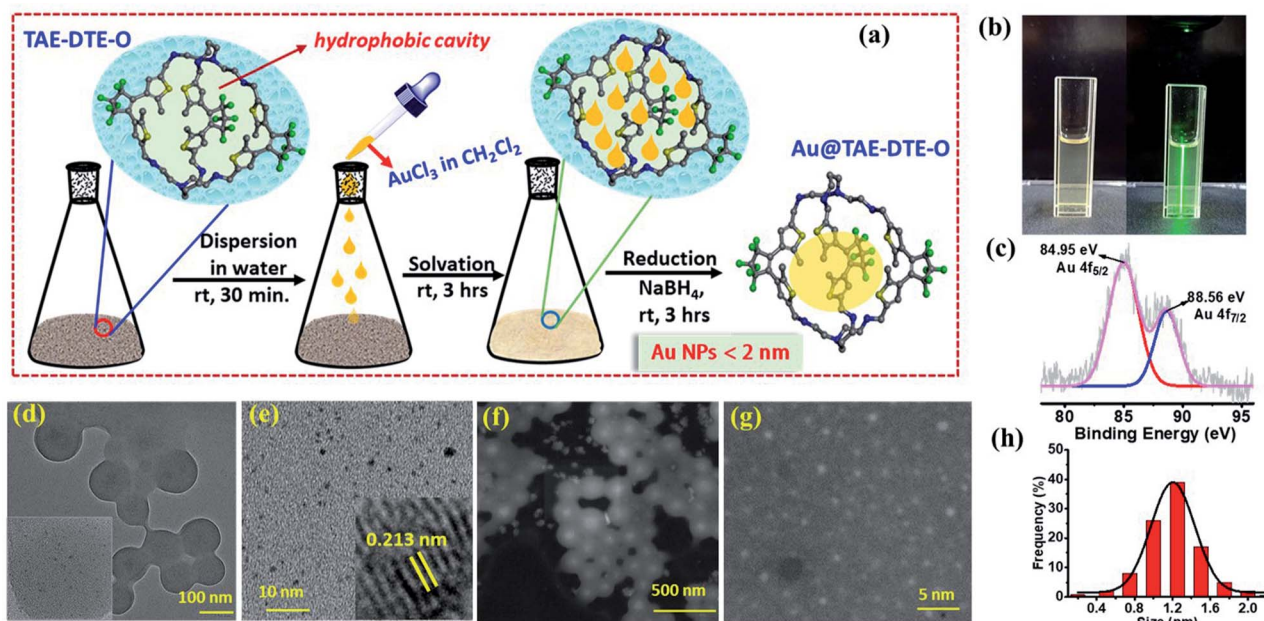


Fig. 2 (a) Schematic representation for *in situ* growth and stabilization of ultrasmall gold nanoparticles (Au NPs) inside the organic cage. (b) Au@TAE-DTE-O in acetonitrile (left) and the Tyndall effect for the same sample (right). (c) Deconvoluted XPS spectrum for Au NPs. Morphology of Au@TAE-DTE-O: (d) low resolution TEM image (inset shows Au NPs inside spheres); (e) high resolution TEM image (inset picture shows lattice fringes); HAADF-STEM images: (f) low resolution and (g) high resolution. (h) Histogram for the particle size of Au NPs obtained by HAADF-STEM.

morphology (~ 150 nm), wherein the gold metal NPs were embedded inside the spheres (Fig. 2f). The high resolution HAADF-STEM images of Au@TAE-DTE-O exhibited uniform dispersion of the ultrafine Au NP matrix (Fig. 2g) and correspondingly, the average diameter of Au NPs was found to be ~ 1.3 nm (Fig. 2h). The elemental mapping indicated the uniform distribution of Au, S, C, N, and F in the Au@TAE-DTE hybrid (Fig. S17[†]). Notably, the absence of the chlorine element (Cl) corresponds to the gold salt ensuring the presence of metallic gold rather than the ionic one. The energy dispersive X-ray (EDX) study demonstrated 2.2% Au NPs in Au@TAE-DTE-O, which is in agreement with that found by the ICP-AES analysis (Fig. S18[†]). Next, X-ray photoelectron spectroscopy (XPS) study was performed on the Au@TAE-DTE-O. Importantly, two peaks at 84.95 eV and 88.56 eV represented two distinct spin-orbit pairs, Au 4f_{5/2} and Au 4f_{7/2}, respectively, confirming the presence of metallic gold (Au(0)) in the POC (Fig. 2c).⁴⁵ Notably, the negative core level shift in the XPS spectrum of Au(0) as compared to the literature report²⁹ further justified the downsizing of the Au NPs.⁴⁶ Deconvolution of the XPS spectra of Au@TAE-DTE-O also showed signature peaks for other elements such as sulphur (154.37 eV and 164.43 eV), carbon (285.73 eV and 286.81 eV), nitrogen (400.5 eV) and fluorine (689.25 eV) (Fig. S19[†]).

The photochromic behaviour and UV-Vis absorption spectra of Au@TAE-DTE-O and Au@TAE-DTE-C were found to be similar to those of the TAE-DTE-O and TAE-DTE-C, respectively, indicating that the intrinsic photochromic properties of the POC are unaffected by the Au NPs (Fig. S20[†]). However, we did not observe any additional plasmon absorption band for Au NPs, which can be attributed to the smaller sizes of the NPs, and a similar observation has been reported earlier as well.^{6,47} Owing to the wide absorption and presence of ultra-small Au NPs, the Au@TAE-DTE hybrid could be a promising photocatalyst for the CO₂ reduction reaction.

We performed Mott Schottky (MS) analysis to assess the viability of the TAE-DTE-O for the photocatalytic CO₂ reduction (see the ESI, Fig. 3a). The MS measurements were carried out at different frequencies and the positive slope of the obtained C⁻² values (*vs.* the applied potential) suggested the typical n-type semiconductor nature of the TAE-DTE-O. The flat band potential for TAE-DTE-O was found to be -0.92 V w.r.t. the RHE at pH = 7 which was more negative than the reduction potential of CO₂ to CO (-0.52 V *vs.* NHE) as well as CH₄ (-0.24 V *vs.* NHE) (Fig. 3b). Electronic band structures *vs.* RHE at pH = 7 were elucidated for TAE-DTE-O on the basis of the bandgap and flat band positions. This clearly indicates the feasibility of the TAE-DTE-O to carry out the CO₂ reduction reaction (Fig. 3b).

Next, we evaluated the potential of the Au@TAE-DTE hybrid for photocatalytic CO₂ reduction in a CO₂ saturated solution of CH₃CN and H₂O (3 : 1 ratio) using triethylamine (TEA) as a sacrificial hole scavenging agent (see the ESI[†]). The amount of the photo reduced products was quantified by GC-MS analysis. Visible light ($\lambda > 400$ nm) driven CO₂ reduction performed with the Au@TAE-DTE-O showed the formation of $620 \mu\text{mol g}^{-1}$ CO in 11 hours with an average rate of $56.4 \mu\text{mol g}^{-1} \text{h}^{-1}$ (Fig. 3d). Notably, a small amount of CH₄ ($135 \mu\text{mol g}^{-1}$ in 11 hours) and

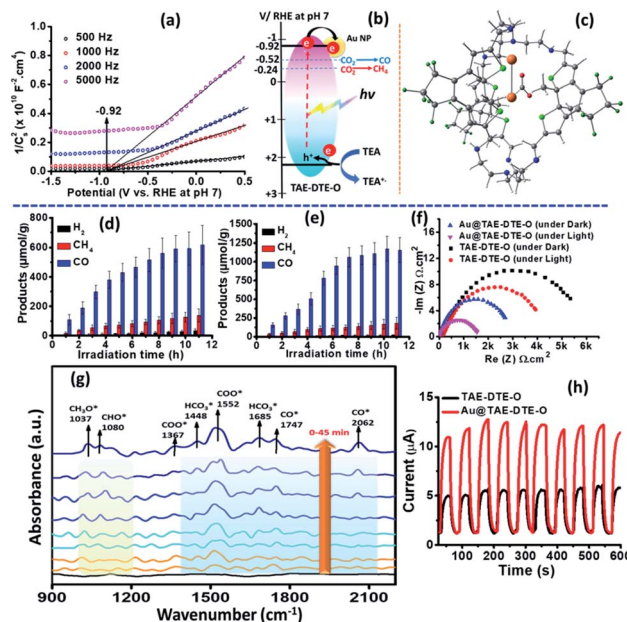


Fig. 3 Photochemical CO₂ reduction: (a) Mott–Schottky plot for TAE-DTE-O at different frequencies. (b) Bandgap alignment to illustrate the feasibility of the materials for catalyzing the CO₂ reduction reaction. (c) Optimized CO₂ binding site on Au@TAE-DTE-C. CO₂ reduction reaction using Au@TAE-DTE-O under (d) visible light (400–750 nm) and (e) full-range light (250–750 nm). (f) Nyquist plot for charge transfer resistance under light and dark conditions. (g) *In situ* FT-IR experiment for CO₂ reduction using Au@TAE-DTE-O under visible light irradiation. (h) Photocurrent graph under light and dark conditions.

a negligible amount of H₂ gas ($39 \mu\text{mol g}^{-1}$ in 11 hours) were also detected. However, the selectivity for CO, CH₄ and H₂ formation was calculated to be 78.3%, 17.4%, and 4.3%, respectively. Importantly, GC-MS analysis of the liquid aliquot of the reaction mixture confirmed the absence of liquid products such as HCOOH, HCHO or CH₃OH as a result of CO₂ reduction. Next, the CO₂ reduction experiment was performed upon irradiating with light of the full range (250–750 nm). Interestingly, almost double the amount of CO formation ($1157 \mu\text{mol g}^{-1}$ in 11 hours) with a rate of $105.18 \mu\text{mol g}^{-1} \text{h}^{-1}$ was detected with the full range irradiation (Fig. 3e). At the same time, a small amount of CH₄ ($185 \mu\text{mol g}^{-1}$ in 11 hours) and insignificant amount of H₂ ($21 \mu\text{mol g}^{-1}$ in 11 hours) were also observed along with CO formation. Notably, the selectivity of the CO formation is noted to be impressive, and the relative percentage of CO, CH₄ and H₂ formation was found to be 85.1%, 13.4%, and 1.5%, respectively. In order to understand the substantially enhanced catalytic activity of Au@TAE-DTE-O in full-range light, we have recorded the UV-Vis absorption spectrum upon irradiating Au@TAE-DTE-O with full-range light (250–750 nm) for 20 minutes (Fig. S21a[†]). This showed the characteristic absorption peaks for both Au@TAE-DTE-O (UV region) and Au@TAE-DTE-C (visible region). The UV-Vis spectrum was also recorded after completion of photocatalysis in full-range light and found to be similar as observed after 20 minutes of irradiation, illustrating that the maximum concentration of photoisomers present in the catalytic medium was

reached within 20 minutes (Fig. S21b†). The percentage of photo-isomers in full-range was calculated based on absorbance in the visible region and found to be 65% (Au@TAE-DTE-O) and 35% (Au@TAE-DTE-C) (Fig. S21c & d†). However, the existence of a mixture of photoisomers in the full-range coherently resulted in a wide-range of absorbance from the UV to the visible region that subsequently exhibited better CO₂ reduction as compared to individual visible or UV light irradiation. Interestingly, cumulative absorbance of photoisomers was nicely covered under the global solar spectrum (Fig. S21c†). Next, an isotopic labelling experiment performed under a ¹³CO₂ atmosphere for the Au@TAE-DTE-O hybrid confirmed that the produced CO and CH₄ originated from CO₂ (Fig. S22 & S23†). Importantly, the real-time progress of the CO₂ reduction reaction was monitored by *in situ* experiments using Diffuse Reflectance Infrared Fourier Transform spectroscopy (DRIFTS) (Fig. 3g).⁴⁸ The DRIFT spectra were recorded at a time interval of 5 minutes upon continuous visible light irradiation. Two peaks were detected at 1552 cm⁻¹ and 1367 cm⁻¹ for the COOH* and COO* intermediates, respectively, which were characteristic intermediates for the CO/CH₄ formation.⁴⁹ Peaks at 1463 cm⁻¹ and 1685 cm⁻¹ could be assigned to the symmetric and asymmetric stretching of the HCO₃^{*}, respectively. Most importantly, stretching and bending vibrations for the surface adsorbed CO* intermediate were observed at 2062 cm⁻¹ and 1748 cm⁻¹.⁴⁸ Notably, increasing intensity of the CO* peak was observed with reaction time, suggesting accumulation of the CO on the catalytic surface. Additionally, two peaks appearing at 1037 cm⁻¹ and 1080 cm⁻¹ were assigned to CH₃O* and CHO*, respectively, which are crucial intermediates formed during CH₄ formation.⁴⁹ Thus, reaction intermediates in the course of CO₂ reduction identified by the DRIFT study clearly indicated CO formation along with a measurable amount of CH₄ as well.

Further, various control experiments were performed to evaluate the role of individual components in the photocatalysis. This has established that the catalyst (Au@TAE-DTE), TEA, CO₂, and light are necessary components in order to realize the photocatalytic CO₂ reduction reaction (Fig. S24†). The photocatalytic experiment was also performed with the recovered Au@TAE-DTE catalyst for four consecutive cycles, and the catalytic activity was found to be retained as observed for the first cycle, indicating the excellent catalytic recyclability (Fig. S25†). TEM analysis of the recovered catalyst displayed a similar morphology as that observed for the as-synthesized Au@TAE-DTE-O, indicating excellent stability of the photocatalyst (Fig. S26†). Further, we have also examined the potential of the as-synthesized cage (TAE-DTE-O) for photocatalytic CO₂ reduction upon irradiating with both visible ($\lambda = 400\text{--}750$ nm) and full range ($\lambda = 250\text{--}750$ nm) light and the corresponding CO formation in 12 hours was observed to be 17 $\mu\text{mol g}^{-1}$ and 360 $\mu\text{mol g}^{-1}$, respectively (Fig. S27†). However, it is noteworthy that the photochemical CO₂ reduction to CO using the photochromic organic cage was observed to be 100% selective and no other product was detected.

The above results unambiguously indicated the important role of the Au NPs in the photocatalytic CO₂ reduction. Moreover, the enhanced photocatalytic activity of the Au@TAE-DTE hybrid

compared to the photochromic organic cage (TAE-DTE) was validated by the excited-state lifetime measurements and charge separation studies (impedance study and photocurrent measurements) (Fig. 3f and h, S28). The excited-state lifetime for both Au@TAE-DTE-C and TAE-DTE-C was measured upon exciting at 510 nm, and the corresponding decay was analyzed at 650 nm (Fig. S28†). The lifetime for TAE-DTE-C and Au@TAE-DTE-C was found to be 1.29 ns and 0.45 ns, respectively (Table S1†). Fast decay after Au NP stabilization is indicative of the fast electron transfer from the cage to the Au centre, supporting the enhanced catalytic activity of Au@TAE-DTE-C. Next, the lower resistance for Au@TAE-DTE-C/TAE-DTE-C (DTE closed form) compared to Au@TAE-DTE-O/TAE-DTE-O noted in the impedance study implies the smaller electron transfer resistance due to the enhanced π conjugation in the former case. Notably, both the photo-isomers of the Au@TAE-DTE hybrid exhibited a smaller semi-circle radius compared to their corresponding photo-isomers of bare cages, indicative of lower charge-transfer resistance after Au NP encapsulation (Fig. 3f). The photocurrent for Au@TAE-DTE-O under visible light irradiation was around 2.5 times higher compared to the pristine TAE-DTE-O cage, corroborating the formation of the Au \cdots TAE-DTE Schottky junction that could have helped to separate the photogenerated electron-hole pairs and subsequently result in higher charge transfer efficiency from the cage to Au NPs in the Au@TAE-DTE-O hybrid (Fig. 3h).

The experimental results clearly demonstrated that the Au NPs play a crucial role in the photocatalytic CO₂ reduction. Therefore, we optimized the model structure for the Au NP stabilized POC to evaluate the thermodynamic feasibility and catalytic centre in the Au@TAE-DTE for the CO₂ reduction reaction (see the ESI, Fig. S29†). The DFT computational investigation was performed at the D3-B3LYP/6-31G(d) level, and two gold atoms were considered for the optimization in the cavity of TAE-DTE-O and TAE-DTE-C, in view of reducing the computational cost.⁵⁰ The study revealed that the cavity of TAE-DTE-O and TAE-DTE-C was able to stabilize Au atoms by releasing 1.69 and 1.71 kcal mol⁻¹ of free energy, respectively, *via* the non-bonding weak interactions from N and S atoms (Fig. S29†). More importantly, the CO₂ adsorption site in Au@TAE-DTE-C was found to be thermodynamically favourable by 6.20 kcal mol⁻¹ at the Au centre and therefore likely to act as a catalytic centre during the CO₂ reduction (Fig. 3c). This was further supported by the fact that the LUMO of the gold nanoparticles was found to be of lower energy as compared to the LUMO of the POC (TAE-DTE-O/TAE-DTE-C) which illustrates facile electron transfer from the POC to the Au centre (Fig. S30†). The possible catalytic site at the bare TAE-DTE-C was also determined by performing DFT calculations considering individual hetero-atoms of the POC as the CO₂ binding sites. The secondary nitrogen of the TAE-DTE-C was observed to be the energetically most favourable binding site for the CO₂ molecule (Fig. S31†).

Conclusions

In conclusion, we have utilized a photochromic organic cage (TAE-DTE) as a platform for the *in situ* growth and stabilization

of ultra-small (<2 nm) gold nanoparticles (Au@TAE-DTE) via the reverse double salt approach (RDSA). The photochromic and absorption properties of the Au@TAE-DTE hybrid were observed to be similar to those of the bare POC. The highly dispersed Au@TAE-DTE-O material acted as a visible light ($\lambda = 400\text{--}750\text{ nm}$) driven photocatalyst for CO₂ reduction to CO with moderate yield (617 μmol). Interestingly, tuning the irradiation light ($\lambda = 250\text{--}750\text{ nm}$) resulted in the formation of both photoisomers of Au@TAE-DTE and therefore displayed significantly enhanced photocatalytic activity (1178 μmol) and selectivity. This work will pave the way towards developing state-of-the-art photocatalysts for CO₂ reduction by tuning the light-absorbing properties of the material.

Conflicts of interest

There are no conflicts to declare.

Acknowledgements

TKM acknowledges the SERB, Dept. of Science and Technology (DST), Govt. of India for financial support (project no. CRG/2019/005951). AS thanks the SERB for funding. PV acknowledges the Council of Scientific and Industrial Research (CSIR), Govt. of India, for the fellowship.

Notes and references

- 1 T. Yasukawa, H. Miyamura and S. Kobayashi, *Chem. Soc. Rev.*, 2014, **43**, 1450–1461.
- 2 E. Auyeung, W. Morris, J. E. Mondloch, J. T. Hupp, O. K. Farha and C. A. Mirkin, *J. Am. Chem. Soc.*, 2015, **137**, 1658–1662.
- 3 G. C. Bleier, J. Watt, C. K. Simocko, J. M. Lavin and D. L. Huber, *Angew. Chem., Int. Ed.*, 2018, **57**, 7678–7681.
- 4 W. Heni, L. Vonna and H. Haidara, *Nano Lett.*, 2015, **15**, 442–449.
- 5 Y. Deng, Z. Zhang, P. Du, X. Ning, Y. Wang, D. Zhang, J. Liu, S. Zhang and X. Lu, *Angew. Chem., Int. Ed.*, 2020, **59**, 6082–6089.
- 6 Z. Luo, X. Yuan, Y. Yu, Q. Zhang, D. T. Leong, J. Y. Lee and J. Xie, *J. Am. Chem. Soc.*, 2012, **134**, 16662–16670.
- 7 Z. Wu, Q. Yao, O. J. H. Chai, N. Ding, W. Xu, S. Zang and J. Xie, *Angew. Chem., Int. Ed.*, 2020, **132**, 10020–10025.
- 8 L. An, D. Zhang, L. Zhang and G. Feng, *Nanoscale*, 2019, **11**, 9563–9573.
- 9 M. Zhao, K. Deng, L. He, Y. Liu, G. Li, H. Zhao and Z. Tang, *J. Am. Chem. Soc.*, 2014, **136**, 1738–1741.
- 10 P. Pachfule, S. Kandambeth, D. D. Diaz and R. Banerjee, *Chem. Commun.*, 2014, **50**, 3169–3172.
- 11 L. He, F. Weniger, H. Neumann and M. Beller, *Angew. Chem., Int. Ed.*, 2016, **55**, 12582–12594.
- 12 A. Dhakshinamoorthy and H. Garcia, *Chem. Soc. Rev.*, 2012, **41**, 5262–5284.
- 13 R. Žalneravičius, A. Mikalauskaitė, G. Niaura, A. Paškevičius and A. Jagminas, *Mater. Sci. Eng. C*, 2019, **102**, 646–652.
- 14 M. Cabrero-Antonino, S. Remiro-Buenamanana, M. Souto, A. A. Garcia-Valdivia, D. Choquesillo-Lazarte, S. Navalon, A. Rodriguez-Dieguez, G. M. Espallargas and H. Garcia, *Chem. Commun.*, 2019, **55**, 10932–10935.
- 15 B. Mondal and P. S. Mukherjee, *J. Am. Chem. Soc.*, 2018, **140**, 12592–12601.
- 16 Y. Yang, T. Wang, X. Jing and G. Zhu, *J. Mater. Chem. A*, 2019, **7**, 10004–10009.
- 17 X. Yang, J.-K. Sun, M. Kitta, H. Pang and Q. Xu, *Nat. Catal.*, 2018, **1**, 214–220.
- 18 T. Hasell and A. I. Cooper, *Nat. Rev. Mater.*, 2016, 16053–16066.
- 19 T. Tozawa, J. T. A. Jones, S. I. Swamy, S. Jiang, D. J. Adams, S. Shakespeare, R. Clowes, D. Bradshaw, T. Hasell, S. Y. Chong, C. Tang, S. Thompson, J. Parker, A. Trewin, J. Bacsá, A. M. Z. Slawin, A. Steiner and A. I. Cooper, *Nat. Mater.*, 2009, **8**, 973–978.
- 20 Y.-N. Gong, W. Zhong, Y. Li, Y. Qiu, L. Zheng, J. Jiang and H.-L. Jiang, *J. Am. Chem. Soc.*, 2020, **142**, 16723–16731.
- 21 M. F. Kuehnle, K. L. Orchard, K. E. Dalle and E. Reisner, *J. Am. Chem. Soc.*, 2017, **139**, 7217–7223.
- 22 W. Kim, B. A. McClure, E. Edri and H. Frei, *Chem. Soc. Rev.*, 2016, **45**, 3221–3243.
- 23 C. Cometto, R. Kuriki, L. Chen, K. Maeda, T.-C. Lau, O. Ishitani and M. Robert, *J. Am. Chem. Soc.*, 2018, **140**, 7437–7440.
- 24 T. Kong, Y. Jiang and Y. Xiong, *Chem. Soc. Rev.*, 2020, **49**, 6579–6591.
- 25 D. Li, M. Kassymova, X. Cai, S.-Q. Zang and H.-L. Jiang, *Coord. Chem. Rev.*, 2020, **412**, 213262–213277.
- 26 C. Dai, L. Zhong, X. Gong, L. Zeng, C. Xue, S. Li and B. Liu, *Green Chem.*, 2019, **21**, 6606–6610.
- 27 F. M. Wisser, M. Duguet, Q. Perrinet, A. C. Ghosh, M. Alves-Favaro, Y. Mohr, C. Lorentz, E. A. Quadrelli, R. Palkovits, D. Farrusseng, C. Mellot-Draznieks, V. d. Waele and J. m. Canivet, *Angew. Chem., Int. Ed.*, 2020, **59**, 5116–5122.
- 28 X. Chang, T. Wang and J. Gong, *Energy Environ. Sci.*, 2016, **9**, 2177–2196.
- 29 Q.-T. Fu, X. Yan, X.-Y. Zhang, Y. He, W.-D. Zhang, Y. Liu, Y. Li and Z.-G. Gu, *Dalton Trans.*, 2020, **49**, 12145–12149.
- 30 J.-S. Wang, K. Wu, C. Yin, K. Li, Y. Huang, J. Ruan, X. Feng, P. Hu and C.-Y. Su, *Nat. Commun.*, 2020, **11**, 4675.
- 31 M. Irie, T. Fukaminato, K. Matsuda and S. Kobatake, *Chem. Rev.*, 2014, **114**, 12174–12277.
- 32 G. M. Peters and J. D. Tovar, *J. Am. Chem. Soc.*, 2019, **141**, 3146–3152.
- 33 W. Li, X. Li, Y. Xie, Y. Wu, M. Li, X.-Y. Wu, W.-H. Zhu and H. Tian, *Sci. Rep.*, 2015, **5**, 9186–9192.
- 34 R.-J. Li, M. Han, J. Tessarolo, J. J. Holstein, J. Lübben, B. Dittrich, C. Volkmann, M. Finze, C. Jenne and G. H. Clever, *ChemPhotoChem*, 2019, **3**, 378–383.
- 35 Y. Gu, E. A. Alt, H. Wang, X. Li, A. P. Willard and J. A. Johnson, *Nature*, 2018, **560**, 65–69.
- 36 A. Singh, P. Verma, S. Laha, D. Samanta, S. Roy and T. K. Maji, *ACS Appl. Mater. Interfaces*, 2020, **12**, 20991–20997.

- 37 P. Verma, A. Singh and T. K. Maji, *Chem. Sci.*, 2021, DOI: 10.1039/d0sc05721e.
- 38 D. Roke, C. Stuckhardt, W. Danowski, S. J. Wezenberg and B. L. Feringa, *Angew. Chem., Int. Ed.*, 2018, **57**, 10515–10519.
- 39 H. S. Lee, S. Jee, R. Kim, H.-T. Bui, B. Kim, J.-K. Kim, K. S. Park, W. Choi, W. Kim and K. M. Choi, *Energy Environ. Sci.*, 2020, **13**, 519–526.
- 40 A. Villa, N. Dimitratos, C. E. Chan-Thaw, C. Hammond, G. M. Veith, D. Wang, M. Manzoli, L. Pratia and G. J. Hutchings, *Chem. Soc. Rev.*, 2016, **45**, 4953–4994.
- 41 S. Tian, Y. Cao, T. Chen, S. Zang and J. Xie, *Chem. Commun.*, 2020, **56**, 1163–1174.
- 42 S.-i. Noro and T. Nakamura, *NPG Asia Mater.*, 2017, **9**, 1–14.
- 43 U. Ulmer, T. Dingle, P. N. Duchesne, R. H. Morris, A. Tavasoli, T. Wood and G. A. Ozin, *Nat. Commun.*, 2019, **10**, 3169–3180.
- 44 G. S. Ghodake, N. G. Deshpande, Y. P. Lee and E. S. Jin, *Colloids Surf., B*, 2010, **75**, 584–589.
- 45 M. H. Engelhard, J. N. Smith and D. R. Baer, *Surf. Sci. Spectra*, 2016, **23**, 29–39.
- 46 I. Aruna, B. R. Mehta, L. K. Malhotra and S. M. Shivaprasad, *J. Appl. Phys.*, 2008, **104**, 64308–64312.
- 47 S. Banerjee, N. Preeyanka, H. Dey, S. Seth, A. Rahaman and M. Sarkar, *J. Phys. Chem. C*, 2020, **124**, 5009–5020.
- 48 X. Yu, Z. Yang, B. Qiu, S. Guo, P. Yang, B. Yu, H. Zhang, Y. Zhao, X. Yang, B. Han and Z. Liu, *Angew. Chem., Int. Ed.*, 2019, **58**, 632–636.
- 49 X. Li, Y. Sun, J. Xu, Y. Shao, J. Wu, X. Xu, Y. Pan, H. Ju, J. Zhu and Y. Xie, *Nat. Energy*, 2019, **4**, 690–699.
- 50 M. E. Hafez, H. Ma, W. Ma and Y.-T. Long, *Angew. Chem., Int. Ed.*, 2019, **58**, 6327–6332.